

Dynamics of femtosecond ablation on thin Au film

S.A. Wolbers, BSc

Supervision:

Prof. Dr. J.I. Dijkhuis

Dr. D. van Oosten

Prof. Dr. D.M. Krol

at Utrecht University

August 15, 2013



Universiteit Utrecht

Contents

Contents	2
1 Introduction	3
2 Theory	4
2.1 FDTD	5
2.2 Metallic properties	13
2.3 Diffusion	15
3 Experimental setup	18
4 Results	21
4.1 Self reflectivity	21
4.2 Morphology	23
5 Transmission spectroscopy	29
5.1 Theory	29
5.2 Setup	30
5.3 Results	32
6 Conclusion	35
7 Dankwoord	36
8 Appendix	37
References	48

1 Introduction

Femtosecond ablation is becoming of great importance in machining of micron or sub micron structures in dielectrics^[1], semiconductors^[2] and metals^[3]. One of the applications in nanomachining is the creation of waveguides for light, which can cause a non-trivial transmission profile due to the creation of surface plasmons^[4]. However, before we can study these possibilities we first need to understand the dynamics of femtosecond ablation. Our main question will thus be,

Which processes can accurately describe the dynamics of femtosecond ablation on thin gold films?

Different approaches have been made to describe the processes, including the two-temperature model^[5] (TTM). The two-temperature model makes the distinction between the heating of electrons and the lattice. It assumes that light coming from the laser is heating the electrons first, which in turn dispense their heat to the lattice. However, the deposition of energy by the laser using an intensity profile^[6] is often too simplistic as it does not incorporate non-linear effects due to the narrow focusing. One of the goals in this report is to find out how the energy deposition works for narrow focusing femtosecond ablation. We study this process by describing the process with the Finite-Difference Time-Domain (FDTD) method^[7] in combination with assuming Drude-like behaviour of the electrons in the excited region of the sample. This method will simulate the deposition of the laser energy, which then can be verified by performing experiments where the self reflectivity of the laser pulses are measured. One of the sub questions is thus,

How is self reflectivity on thin gold films effected by femtosecond laser pulses?

Once we quantified the energy deposition of the laser pulses, we consider heat diffusion to find the spread of deposited energy over the sample. By establishing a possible number of ablation criteria we can then simulate the geometry of the ablated holes. Again, these results can be compared with experimental results, where holes are ablated with a range of laser fluences.

What is the criterion for ablation with femtosecond laser pulses in thin gold films?

As the main application of these holes is the creation of a waveguide it is useful to study the ablated samples in a larger scope. Particularly interesting is performing transmission spectroscopy over a large spectral range with holes ablated through the entire film. In section 5 the use of a white light laser in combination with an computer driven AOTF for high speed (μs) transmission spectroscopy is discussed.

2 Theory

There is quite some uncertainty over the way ablation works^[8]. One of the theories proposed for dealing with the problem is the so-called two-temperature model. The model assumes the energy to be absorbed by the electrons first, followed by an equilibration between the electrons and the lattice. Atoms do not directly interact with light as the atoms are too heavy.

In a semiconductor the absorption of the laser energy by a valence electron will result in the creation of free carriers in the conduction band. Important processes in the excitation of most semiconductors are the one- and two-photon absorption and the impact ionization^[9]. If the energy of the laser is large enough and sufficient free carriers are created a plasma is formed and will have metal-like behaviour.

In a metal however there are already sufficient free carriers, which means that the laser energy will be directly absorbed by the free carriers, resulting in heating. The difference in heat between the electrons and lattice can be expressed by its temperatures. The diffusion of this heat, combined with the coupling between electrons and lattice and the input of the laser energy can be described with the two-temperature model. The model has two differential equations for the electron (T_e) and lattice (T_l) temperatures in space (\vec{r}) and time (t),

$$C_e \frac{\partial T_e}{\partial t} = \nabla \cdot (K_e(T_e) \nabla T_e) - G(T_e - T_l) + S(\vec{r}, t) \quad (2.1)$$

$$C_l \frac{\partial T_l}{\partial t} = \nabla \cdot (K_l(T_l) \nabla T_l) + G(T_e - T_l) \quad (2.2)$$

Here, C_e and C_l are the heat capacities of the electrons and lattice, respectively, K_e and K_l the heat conductivities of the electrons and lattice, respectively, G the coupling term between the electrons and the lattice (phonons) and S a source term, in our case the energy delivered by the laser.

Though the energy deposition by the laser and the electron diffusion have some overlap in time, there is a clear distinction in speed. The ablation process can be divided into two time regimes: the energy deposition by the laser (I) followed by the temperature diffusion and coupling between the electrons and the lattice (II). In the first regime, which is roughly the first 1 ps, the most significant effect is the deposition of laser energy. During this transfer the properties of the material will change drastically due to the rapid deposition of energy. This happens so fast that even within the laser pulse of roughly 100 fs the material is changing, at least under ablation conditions. In section 2.1 the principle of FDTD is discussed to describe the process of deposition and in section 2.2 the effect of the deposited energy on the material will be explained, causing a change in reflectivity and possible scattering of hot electrons.

In the second regime (1 - 100 ps) the energy deposition from the incident laser pulse is complete and the diffusion and electron-phonon coupling become the dominant processes. While the heat of the electrons is diffusing through the material the electrons will also exchange heat with the lattice due to the coupling, causing the lattice temperature to rise and the electron temperature to fall. Eventually, the electrons and lattice will reach an equilibrium temperature depending on the initial temperature difference. In section 2.3 we will see how the diffusion and the ablation criteria affects the shape of the ablated holes.

2.1 FDTD

The problem with simulating the deposition of the laser pulse energy is that the details of focusing a laser beam are quite complex. If the laser would not be focused, an Gaussian intensity profile could be used to describe the energy transfer (see appendix A). However, as non-linear effects will occur when focusing sharply, the effects are to be described by Maxwell's equations. In particular, two equations are important: Ampère's and Faraday's laws,

$$\nabla \times \vec{E} = -\mu_0 \frac{\partial \vec{H}}{\partial t} \quad (2.3)$$

$$\nabla \times \vec{H} = \sigma \vec{E} + \epsilon \frac{\partial \vec{E}}{\partial t} \quad (2.4)$$

These equations state that the spatial variation of the electric field \vec{E} is dependent on the time variation of the magnetizing field \vec{H} and vice versa. Here σ is the electrical conductivity, $\epsilon = \epsilon_0 \epsilon_r$ the permittivity and μ the permeability. Equation 2.4 can be rewritten introducing the electrical displacement field \vec{D} ^[10],

$$\nabla \times \vec{H} = \frac{\partial \vec{D}}{\partial t} \quad (2.5)$$

$$\vec{D}(\omega) = \epsilon_0 \epsilon_r^* \vec{E}(\omega). \quad (2.6)$$

D and E will be normalized to Gaussian units for simplicity in the formulas,

$$\tilde{E} = \sqrt{\frac{\epsilon_0}{\mu_0}} E, \quad (2.7)$$

$$\tilde{D} = \sqrt{\frac{1}{\epsilon_0 \mu_0}} D. \quad (2.8)$$

Equations 2.3, 2.5 and 2.6 will become,

$$\nabla \times \tilde{E} = -\sqrt{\epsilon_0\mu_0} \frac{\partial \tilde{H}}{\partial t}, \quad (2.9)$$

$$\nabla \times \tilde{H} = \sqrt{\epsilon_0\mu_0} \frac{\partial \tilde{D}}{\partial t}, \quad (2.10)$$

$$\tilde{D} = \epsilon_r^* \tilde{E}. \quad (2.11)$$

From now on, when E and D are used, they will be in Gaussian units, unless specified otherwise.

The D and E field are in the frequency domain, but the simulation uses time-dependent functions thus both needs to be converted to the time domain. First, we will find $\epsilon_r(t)$ (see equation 2.64) by Fourier transforming ϵ_r^* to the time domain (see appendix B.1).

$$\begin{aligned} \epsilon_r^*(\omega) &= \epsilon_\infty - \frac{\omega_p^2}{\omega^2 - i\omega\gamma} \\ \epsilon_r(t) &= \epsilon_\infty + \frac{\omega_p^2}{\gamma} [1 - e^{-\gamma t}] u(t) \quad \text{with :} \\ u(t) &= 0 \text{ for } t < 0 \\ u(t) &= 1 \text{ for } t \geq 0 \end{aligned} \quad (2.12)$$

The D -field now can be converted to the time domain using $\epsilon_r(t)$ and convolution. The expression will be split in three terms: the E -term, I -term and S -term.

$$\vec{D}(t) = \epsilon_r * E(t) \quad (2.13)$$

$$\vec{D}(t) = \epsilon_\infty \vec{E}(t) + \frac{\omega_p^2}{\gamma} u(t) * \vec{E}(t) - \frac{\omega_p^2}{\gamma} e^{-\gamma t} u(t) * \vec{E}(t) \quad (2.14)$$

$$\vec{D}(t) = \epsilon_\infty \vec{E}(t) + \frac{\sigma}{\epsilon_0} u(t) * \vec{E}(t) + \chi_1 \cdot \gamma e^{-\gamma t} u(t) * \vec{E}(t) \quad (2.15)$$

$$\vec{D}(t) = \epsilon_\infty \vec{E}(t) + \vec{I}(t) + \vec{S}(t) \quad (2.16)$$

$$(2.17)$$

Here, $\sigma = \frac{\omega_p^2}{\gamma} \epsilon_0$ and $\chi_1 = -\omega_p^2 \gamma^2$. The E -term (blue) remains the same after the inverse Fourier transform. The I - (green) and S -term (yellow) however, will not. The discrete form will become (see full derivation in appendix B.2),

$$D^n = \epsilon_r E^n + I^n + S^n \quad (2.18)$$

$$D^n = \epsilon_r^* E^n + \frac{\sigma \cdot \Delta t}{\epsilon_0} E^n + I^{n-1} + \chi_1 \cdot \gamma \Delta t E^n + e^{\gamma \Delta t} S^{n-1} \quad (2.19)$$

E^n can be expressed in terms of D^n , I^{n-1} and S^{n-1} .

$$E^n = \frac{D^n - I^n - e^{-\gamma \Delta t} S^n}{\epsilon_r + \frac{\sigma \cdot \Delta t}{\epsilon_0} + \chi_1 \cdot \gamma \Delta t} \quad (2.20)$$

Where I^n and S^n are given by equations B.12 and B.20. D^n is a discrete $D(t)$, which can be calculated using Faraday's equation (2.10), which in turn can be calculated using Ampère's equation 2.9.

Though the \vec{D} -field is now discretized, this is not yet the case for the Maxwell equations (eq. 2.9 and 2.10). Though it would be nice to do this for three dimensions, for computation time this is too expensive. We will limit ourselves to the 1D and 2D case,

1D

Let us recall the Maxwell equations:

$$\begin{aligned} \nabla \times \vec{E} &= -\sqrt{\epsilon_0 \mu_0} \frac{\partial \vec{H}}{\partial t}, \\ \nabla \times \vec{H} &= \sqrt{\epsilon_0 \mu_0} \frac{\partial \vec{D}}{\partial t}. \end{aligned}$$

The direction of propagation is \hat{z} and we choose \vec{D} to be in the x -direction. \vec{H} will then be in the y -direction.

$$\frac{\partial \vec{D}_x}{\partial t} = -\frac{1}{\sqrt{\epsilon_0 \mu_0}} \frac{\partial H_y}{\partial z} \quad (2.21)$$

$$\frac{\partial \vec{H}_y}{\partial t} = -\frac{1}{\sqrt{\epsilon_0 \mu_0}} \frac{\partial E_x}{\partial z} \quad (2.22)$$

In discrete form this becomes,

$$D^n = D^{n-1} - \frac{\Delta t}{\Delta z} \frac{1}{\sqrt{\epsilon_0 \mu_0}} \left[H_{y+\frac{1}{2}}^{n-1} - H_{y-\frac{1}{2}}^{n-1} \right] \quad (2.23)$$

$$H^n = H^{n-1} - \frac{\Delta t}{\Delta z} \frac{1}{\sqrt{\epsilon_0 \mu_0}} \left[E_{x+1}^{n-1} - E_y^{n-1} \right] \quad (2.24)$$

An important aspect of FDTD simulation is that the step size in space and time needs to be linked by the Courant Condition^[10]. In this thesis the relation between Δt and Δz , following the condition will be,

$$\Delta t = \frac{\Delta z}{2 \cdot c} \quad (2.25)$$

Note that $\frac{1}{\sqrt{\epsilon_0 \mu_0}} = c$ and equations 2.23 and 2.24 will become,

$$D_x^{n+\frac{1}{2}} = D_x^{n-\frac{1}{2}} - \frac{1}{2} \left[H_{y+\frac{1}{2}}^n - H_{y-\frac{1}{2}}^n \right] \quad (2.26)$$

$$H_y^{n+\frac{1}{2}} = H_y^{n-\frac{1}{2}} - \frac{1}{2} \left[E_{x+1}^n - E_y^n \right] \quad (2.27)$$

2D

In the 2D we consider the fields in the yz-plane (see figure 2.1), but as the fields are in general 3D we consider two different modes: one where there is no magnetic field in the propagation direction, TM (Transverse Magnetic) and one where there is no electric field in the propagation direction, TE (Transverse Electric). Maxwell's equations will then look like,

TM mode

$$\frac{\partial H_x}{\partial t} = -\frac{1}{\sqrt{\epsilon_0 \mu_0}} \left(\frac{\partial E_z}{\partial y} - \frac{\partial E_y}{\partial z} \right) \quad (2.28)$$

$$\frac{\partial D_y}{\partial t} = \frac{1}{\sqrt{\epsilon_0 \mu_0}} \frac{\partial H_x}{\partial z} \quad (2.29)$$

$$\frac{\partial D_z}{\partial t} = -\frac{1}{\sqrt{\epsilon_0 \mu_0}} \frac{\partial H_x}{\partial y} \quad (2.30)$$

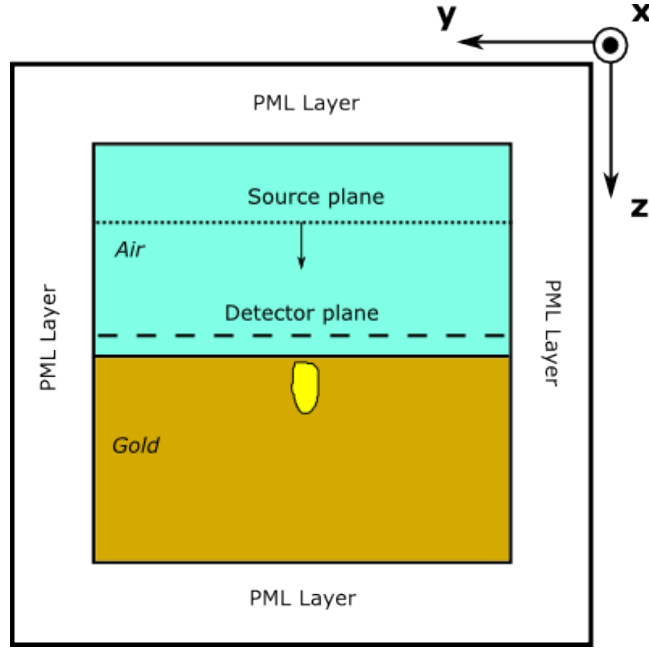


Figure 2.1: 2D FDTD simulation box

In discrete form,

$$H_x^{n+\frac{1}{2}}(j, k) = H_x^{n-\frac{1}{2}}(j, k) + \frac{1}{2} \left[E_z^n(j + \frac{1}{2}, k) - E_z^n(j - \frac{1}{2}, k) - E_y^n(j, k + \frac{1}{2}) + E_y^n(j, k - \frac{1}{2}) \right] \quad (2.31)$$

$$D_y^{n+\frac{1}{2}}(j, k) = D_y^{n-\frac{1}{2}}(j, k) - \frac{1}{2} \left[H_x^n(j, k + \frac{1}{2}) - H_x^n(j, k - \frac{1}{2}) \right] \quad (2.32)$$

$$D_z^{n+\frac{1}{2}}(j, k) = D_z^{n-\frac{1}{2}}(j, k) + \frac{1}{2} \left[H_x^n(j + \frac{1}{2}, k) - H_x^n(j - \frac{1}{2}, k) \right] \quad (2.33)$$

$$(2.34)$$

Note that $\Delta y = \Delta z$ and the Courant condition (eq. 2.25) forms the $\frac{1}{2}$ -factor before the brackets.

TE mode

$$\frac{\partial D_x}{\partial t} = \frac{1}{\sqrt{\epsilon_0 \mu_0}} \left(\frac{\partial H_z}{\partial y} - \frac{\partial H_y}{\partial z} \right) \quad (2.35)$$

$$\frac{\partial H_y}{\partial t} = -\frac{1}{\sqrt{\epsilon_0 \mu_0}} \frac{\partial E_x}{\partial z} \quad (2.36)$$

$$\frac{\partial H_z}{\partial t} = \frac{1}{\sqrt{\epsilon_0 \mu_0}} \frac{\partial E_x}{\partial y} \quad (2.37)$$

In discrete form,

$$D_x^{n+\frac{1}{2}}(j, k) = D_x^{n-\frac{1}{2}}(j, k) + \frac{1}{2} \left[H_z^n(j + \frac{1}{2}, k) - H_z^n(j - \frac{1}{2}, k) - H_y^n(j, k + \frac{1}{2}) + H_y^n(j, k - \frac{1}{2}) \right] \quad (2.38)$$

$$H_y^{n+\frac{1}{2}}(j, k) = H_y^{n-\frac{1}{2}}(j, k) - \frac{1}{2} \left[E_x^n(j, k + \frac{1}{2}) - E_x^n(j, k - \frac{1}{2}) \right] \quad (2.39)$$

$$H_z^{n+\frac{1}{2}}(j, k) = H_z^{n-\frac{1}{2}}(j, k) + \frac{1}{2} \left[E_x^n(j + \frac{1}{2}, k) - E_x^n(j - \frac{1}{2}, k) \right] \quad (2.40)$$

$$(2.41)$$

The result is a set of discrete functions that describe the propagation of electric and magnetic fields. However, the electric field also interacts with the material and creates excitation as described in section 2.2. The temperature of a material depends on the absorbed fluences in the material (more in section 2.2) for which the amplitude of electric field is relevant. Let us consider a monochromatic, electric field,

$$E(t) = E_0 \cos \omega_0 t + \phi \quad (2.42)$$

If we integrate the field over half an optical cycle, we can find an expression for the amplitude and calculate it in our discrete FDTD model,

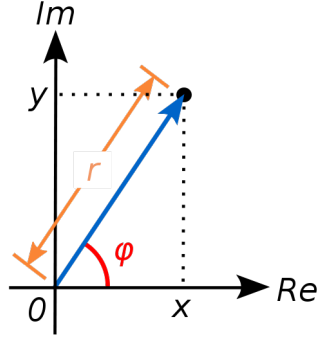


Figure 2.2: Phase of a complex quantity

$$\begin{aligned} \int_0^{T/2} E(t)^2 dt &= \int_0^{T/2} E_0^2 \cos^2 \omega_0 t + \phi dt \\ &= E_0^2 \frac{T}{4} \end{aligned} \quad (2.43)$$

$$E_0 = \sqrt{\frac{2 \int_0^{T/2} E^2(t) dt}{\frac{T}{2}}} \quad (2.44)$$

$$E_0 = \sqrt{\frac{2 \sum_{n=T_0}^{T/2} E^2(n\Delta t) \Delta t}{T/2}} \quad (2.45)$$

We are also interested in the reflectivity, which can be calculated using the time-averaged Poynting vector,

$$\langle S \rangle = \frac{1}{2} \text{Re} \left[\tilde{E}_0 \times \tilde{H}_0^* \right] \quad (2.46)$$

Here \tilde{E}_0 and \tilde{H}_0 are the complex amplitude defined by the amplitude calculated above and the complex phase,

$$\tilde{E}_0 = E_0 e^{-i\phi} \quad (2.47)$$

$$\tilde{H}_0 = H_0 e^{-i\phi} \quad (2.48)$$

However, as we do not now the phase we need a method called ‘homodyne detection’ to extract it from the time-dependent field^[11]. Again, we use an integration over half an optical cycle,

$$\begin{aligned}
& \int_0^{T/2} E(t) e^{-i\omega_0 t} dt = \\
& \int_0^{T/2} E_0 \cos(\omega_0 t + \phi) e^{-i\omega_0 t} dt = \tag{2.49} \\
& \int_0^{T/2} E_0 \cos(\omega_0 t + \phi) [\cos \omega_0 t - i \sin \omega_0 t] dt = \\
& \int_0^{T/2} E_0 \cos(\omega_0 t + \phi) \cos \omega_0 t dt - i \int_0^{T/2} E_0 \cos(\omega_0 t + \phi) \sin \omega_0 t dt = \\
& \frac{E_0 \pi \cos \phi}{2\omega_0} + i \frac{E_0 \pi \sin \phi}{2\omega_0} \tag{2.50}
\end{aligned}$$

The phase of the complex amplitude can be extracted by taking the inverse tangent of the imaginary part over the real part (see figure 2.2).

$$\tilde{\phi} = \tan^{-1} \left[\frac{\sin \phi}{\cos \phi} \right] = \phi \tag{2.51}$$

We can evaluate relation 2.49 in our FDTD simulation and use the result, a complex number to calculate the phase. Now that we both found the amplitude and phase we can calculate the time-averaged Poynting vector with equation 2.46^[12].

$$\langle S \rangle = \frac{1}{2} \text{Re} \left[\tilde{E}_0 \times \tilde{H}_0^* \right]$$

TM mode

$$\langle S \rangle = \frac{1}{2} \text{Re} [0\hat{x} + E_{y0}\hat{y} + E_{z0}\hat{z}] \times (H_{x0}^*\hat{x} + 0\hat{y} + 0\hat{z}) \tag{2.52}$$

$$\langle S \rangle = \frac{1}{2} \text{Re} [-E_{x0}H_{z0}^*] \hat{y} + \frac{1}{2} \text{Re} [E_{x0}H_{y0}^*] \hat{z} \tag{2.53}$$

TE mode

$$\langle S \rangle = \frac{1}{2} \text{Re} [(E_{x0}\hat{x} + 0\hat{y} + 0\hat{z}) \times (0\hat{x} + H_{y0}^*\hat{y} + H_{z0}^*\hat{z})] \tag{2.54}$$

$$\langle S \rangle = \frac{1}{2} \text{Re} [-E_{x0}H_{z0}^*] \hat{y} + \frac{1}{2} \text{Re} [E_{x0}H_{y0}^*] \hat{z} \tag{2.55}$$

Finally, we can use the time-average Poynting vector to calculate the fluence by integrating it over time, both for the reflected (F_R) as the incident (F_I)

case. Dividing the reflected fluence with the incident fluence will give you the reflectivity,

$$F = \int \langle S \rangle dt \quad (2.56)$$

$$R = \frac{F_R}{F_I} \quad (2.57)$$

In short, this subsection, we have used Maxwell's equations to derive a set of discrete equations that describe the propagation of fields within a medium. From the calculated fields we can extract the fields amplitude and the phase, enabling us to calculate the Poynting vector. This vector is then used to determine the reflectivity, and the intensity corresponding to the electric field within the medium.

As we are trying to simulate ablation with a single femtosecond pulse, we have to reconcile that the material is changing during the pulse. This will cause a change in the interaction between the fields and the medium. To know these effects, we need to have a closer look at the metallic properties.

2.2 Metallic properties

First, let us go back to the beginning of this section. There we argued that the temperature of the system will rise when transferring laser energy on a material.

$$C_e \frac{\partial T_e}{\partial t} = \nabla \cdot (K_e(T_e) \nabla T_e) - G(T_e - T_i) + S(\vec{r}, t) \quad (2.58)$$

However, in the first regime, where the deposition of the laser energy takes place, we ignore the coupling between the electrons and phonons and the diffusion of the electron. The simplified equation will then be,

$$C_e \frac{\partial T_e}{\partial t} = S(\vec{r}, t) \quad (2.59)$$

$$C_e \frac{\partial T_e}{\partial t} = \frac{I(\vec{r}, t)}{L_p} \quad (2.60)$$

Here L_p is the skin depth for gold, which will be explained later. The temperature is dependent on the intensity which we can extract from the amplitude of the electric fields,

$$I = \frac{1}{2} n \epsilon_0 c |E|^2 \quad (2.61)$$

Here, I is the intensity, n is the refractive index of the medium, c the speed of light and E the amplitude of the electric field. In the Drude model^[13] a rising temperature will mean that the electron will move faster and thus have a higher change of scattering with each other. This is called damping and can be described with the following relation,

$$\gamma = \frac{1}{\tau_{e-e}} + \frac{1}{\tau_{e-l}} \quad (2.62)$$

where $\frac{1}{\tau_{e-e}} = AT_e^2$ and $\frac{1}{\tau_{e-l}} = BT_l$ ^[14] are the scattering rates for electron-electron and electron-lattice interactions, respectively. A and B are material specific constants and their value for gold can be found in table 2.1 (see appendix C). The scattering rates have a influence on the heat conductivity of the electrons K_e ,

	<i>Au</i>
A	$1.18 \cdot 10^7 \text{ s}^{-1} \text{K}^{-2}$
B	$1.25 \cdot 10^{11} \text{ s}^{-1} \text{K}^{-1}$
K_0	$3.18 \text{ Jm}^{-1} \text{s}^{-1} \text{K}^{-1}$
$\rho \Omega_{vap}$	$32.8 \cdot 10^9 \text{ Jm}^{-3}$
ϵ_∞	6.0
ω_p	$13.8 \cdot 10^3 \text{ THz}$
ω_{pL}	$4.5 \cdot 10^3 \text{ THz}$
ω_0	$4.2 \cdot 10^3 \text{ THz}$
γ_L	$0.9 \cdot 10^3 \text{ THz}$

Table 2.1: Parameters for gold

$$K_e = BK_0 \frac{T_e}{AT_e^2 + BT_l} \quad (2.63)$$

With K_0 the heat conductivity constant for gold found in table 2.1. We note that this equation is only valid for temperatures between the Debye temperature (170 K for gold), and the Fermi temperature ($6.42 \cdot 10^4$ K), the limit^[14]. In our experiment and simulation the temperature is within this range.

The scattering rates have an ever larger influence on the dielectric constant.

$$\epsilon_r^* = \epsilon_\infty - \frac{\omega_p^2}{\omega^2 - i\omega\gamma} \quad (2.64)$$

ϵ_∞ is the standard dielectric constant, ω_p is the plasma frequency, ω is the laser frequency and γ the damping term described by equation 2.62. Appendix D contains more information about the dielectric constant and its derivation.

With the general relation $\epsilon = (n_R + in_I)^2$ it can be seen that a change in the dielectric constant will change the refractive index of the material. This will change the skin depth L_p which affects the deposition of the laser energy. The skin depth reads,

$$L_p \equiv \frac{1}{k_I} = \frac{c}{\omega n_I} \quad (2.65)$$

Here k_I is the imaginary part of the wave vector and c the speed of light. Due to the Gaussian profile of the laser beam, the incoming intensity on the surface of the effect is not homogeneous. This effect is enhanced by the difference in incidence angle due to focusing. In the simulation it is therefore necessary to consider the energy deposition in the yz -plane and not just the z -direction.

As mentioned earlier, a rise in electron (and lattice) temperature will cause a change in the reflectivity of the material. This process is so fast that the material is changing during the pulse. When ablating a material, one can measure the reflected fields and calculate the self-reflectivity of the laser pulse. One can then simulate the energy deposition and calculate the self-reflectivity. If this corresponds with experimental results, it can be assumed that the energy deposition is simulated faithfully after which the effects of diffusion and coupling can be examined.

2.3 Diffusion

In the second regime, realizing that in practice the depth of the film is significantly larger than the skin depth, there will be a large difference in electron temperature between the front and back surface of the metal, causing diffusion. Meanwhile, the electrons will exchange heat with the lattice causing both temperatures to equilibrate.

This diffusion of the electron heat and resulting redistribution of the deposited energy is essential for our ablation model as the temperature is the most important parameter for our ablation criteria. One of these is evaporation, where the ablation depth is given when at any time during the process the temperature fulfils [6],

$$C_l T + C'_e \frac{T^2}{2} \geq \rho \Omega_{vap} \quad (2.66)$$

Here, C_l is the heat capacity of the lattice and C'_e the heat capacity coefficient

($C_e = C'_e T$), T said equilibrium temperature, ρ the material density and Ω_{vap} the mass specific enthalpy of evaporation (see table 2.1). Another criterion can simply be when either the electrons or the phonons reach a certain temperature. An interesting temperature is of course the melting temperature of gold (1337K).

But before we can apply these different criteria we need to know the spreading of temperature by diffusion. To calculate the diffusion we recall equations 2.1 and 2.2,

$$C_e \frac{\partial T_e}{\partial t} = \nabla \cdot (K_e(T_e) \nabla T_e) - G(T_e - T_l) + S(\vec{r}, t)$$

$$C_l \frac{\partial T_l}{\partial t} = \nabla \cdot (K_e(T_e) \nabla T_e) + G(T_e - T_l)$$

This equation can be simplified with certain assumptions. First, using FDTD the source term $S(\vec{r}, t)$ has already been evaluated and has been used to determine the initial condition of T_e . Second, we assume that only the heat of the electrons diffuse over the material and ignore the diffusion term in the phonon equation,

$$C_e \frac{\partial T_e}{\partial t} = \nabla \cdot (K_e(T_e) \nabla T_e) - G(T_e - T_l) \quad (2.67)$$

$$C_l \frac{\partial T_l}{\partial t} = G(T_e - T_l) \quad (2.68)$$

The phonon equation becomes quite straight forward, but the electron equation has the diffusion term which needs to be evaluated. In order to do this we isolate this term and evaluate it first, after which we calculate the coupling between the two systems,

$$C_e(T_e) \frac{\partial T_e}{\partial t} \equiv \nabla \cdot (K_e(T_e) \nabla T_e) \quad (2.69)$$

$$T^{n+1} = T^n + \frac{\Delta t}{C_e(T_e)} (\nabla \cdot (K_e(T^n) \nabla T^n))$$

$$= T^n + \frac{\Delta t}{C_e(T_e)} D(T^n) \quad (2.70)$$

As we only discuss the 1 and 2-dimensional case, the resulting equations become (see full derivation and boundary conditions in append E),

1D

$$D(T) = \frac{\partial}{\partial z} (Ke(T) \frac{\partial T}{\partial z}) \quad (2.71)$$

$$= \frac{1}{\Delta z^2} \left[\frac{Ke(T)_{i+1} + Ke(T)_i}{2} (T_{i+1} - T_i) + \frac{Ke(T)_{i-1} + Ke(T)_i}{2} (T_{i-1} - T_i) \right] \quad (2.72)$$

2D

$$D(T) = \nabla \cdot (Ke(T) \nabla \cdot T) = \frac{\partial}{\partial x} \left(Ke(T) \frac{\partial T}{\partial x} \right) + \frac{\partial}{\partial y} \left(Ke(T) \frac{\partial T}{\partial y} \right) \quad (2.73)$$

$$= \frac{1}{\Delta x^2} \left[\frac{Ke(T)_{i+1} + Ke(T)_i}{2} (T_{i+1} - T_i) + \frac{Ke(T)_{i-1} + Ke(T)_i}{2} (T_{i-1} - T_i) \right] + \quad (2.74)$$

$$\frac{1}{\Delta y^2} \left[\frac{Ke(T)_{j+1} + Ke(T)_j}{2} (T_{j+1} - T_j) + \frac{Ke(T)_{j-1} + Ke(T)_j}{2} (T_{j-1} - T_j) \right] \quad (2.75)$$

Finally, we identified the potential significant processes for ablation. We assume energy of the laser is deposited onto the electrons for heating which can be described by FDTD. During the deposition the material is changing during the pulse, which can be described by the Drude model. The heat of the electrons is diffused over the material and coupled with the lattice. The resulting temperatures can be used for criteria for ablation.

We can now perform experiments, run our simulations and compare both results.

3 Experimental setup

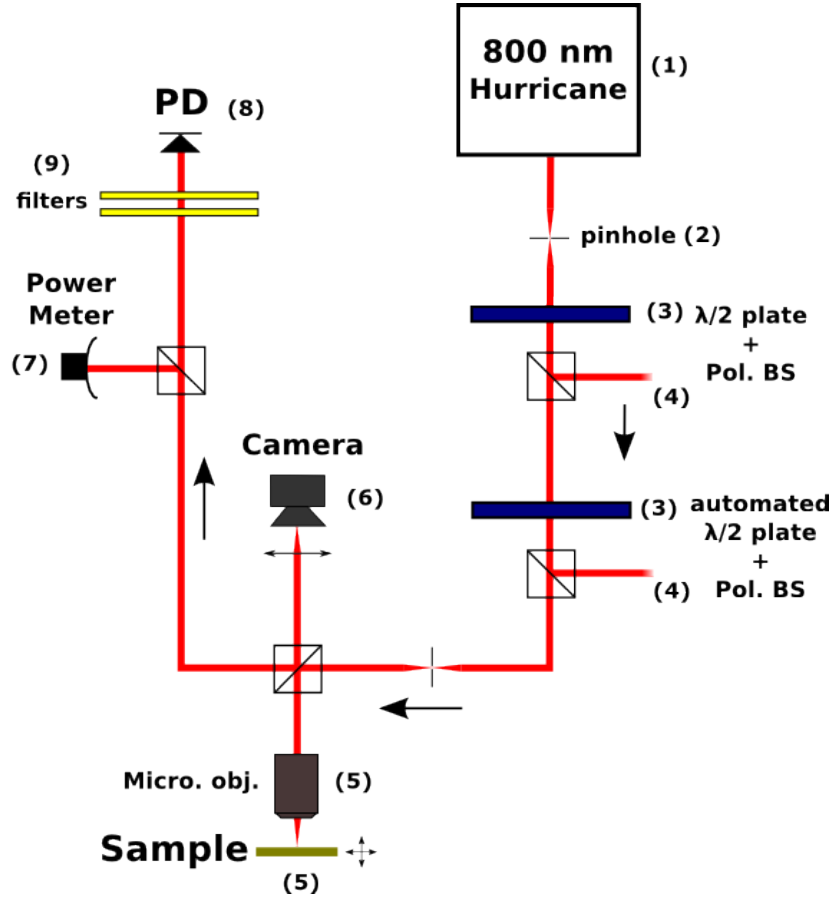


Figure 3.1: Schematic view of setup

The heart of the ablation setup is the Ti:Saph laser, delivering 126fs pulses of 800 nm light with a repetition rate of upto 1 kHz (1). The pulse is then focussed through a pinhole to clean the beam (2) and adopts a nice Gaussian profile. Subsequently, it passes through two sets of a $\lambda/2$ wave plate and a polarizing beam splitter (3 + 4). As the polarizing beam splitter reflects the S-polarized light to a beam dump, the wave plate can control the intensity (P-polarized) light. The first combination is manually controlled and is used for coarse control of the energy input to the setup. The second combination is computer-automated and is used to adjust the energy during the experiment.

The beam is subsequently send through another pinhole to clean the beam after which it is splitted by a beam splitter. The first beam goes to the microscopic objective (5) with an NA of 0.8, which tightly focuses the beam onto a sample (6)

of gold (Au). This is where the actual ablation is done. The sample is mounted on a stage (7) that can be moved and tilted in all three dimensions. The reflected beam from the sample is then sent to a CCD camera for monitoring and measuring the reflectivity *in-situ*. The second beam goes straight through the beam splitter and is used to calibrate how much power is incident on the sample. The beam is therefore splitted again into two, one going to a power meter and one going to a photo diode. The power meter is used to measure the power, but as we need to measure the energy of each single shot we use the photo diode. The diode is connected to an integrator for precise measuring of the pulse energy. Finally, we calibrate the diode to the power meter.

The ablation experiment has two aspects. First, we study the effect of various fluences on the size and shape of the hole. This will be done by shooting an array of 10x10 holes, each shot with a single pulse by adjusting the laser frequency to 1 Hz. For each hole the automated wave plate is rotated to control the incoming fluence. Secondly, we will study the effects in case of overlapping holes by decreasing the intermediate distance and find the limit for independent holes. Unfortunately, during this experiment, the translation stage in the vertical direction broke down, limiting us to shoot the holes over a line only.

List 3.1: Apparatus used in the ablation setup

1. Ti:Sapphire laser (Hurricane, Spectral Physics). 126 fs pulse laser of 800 nm light with a (changeable) repetition rate of upto 1 kHz. The laser is used to ablate thin films of semiconductors or (in this experiment) metals.
2. Pinhole, inserted in between two positive lenses. This combination is used as a spatial filter to clean the beam from noise.
3. $\lambda/2$ -waveplate. This plate is used to rotate the polarization of the light. In combination with a polarizing beam splitter it can be used to couple out laser light from the setup.
4. Polarizing beam splitter. S-polarized light is reflected, P-polarized light is passed through. In combination with the $\lambda/2$ -waveplate it can be used to extract energy from the setup.
5. Microscopic objective. Nikon (CFI160, 100x) with an NA of 0.8
6. Sample. Thin film on glass (in this experiment either 150nm or 400nm) of gold (Au).
7. Translation stage, Zaber Technology (T-LSM025A). Range of 25 mm, with an accuracy of 0.04 μm . Motion can be regulated manually and computer automated.
8. CCD camera. Qimaging RETIGA 1300. The camera is used to analyze the reflection from the sample for alignment and focussing.

9. Power meter. The meter is used to measure the power coming from the laser. During the experiment the meter is not used as its integration time is too slow to measure single shot pulses but calibrates the photo diode.
10. Photo diode. The diode measures the energy of single shot pulses. As the output is in arbitrary units it needs the power meter to be calibrated to.
11. Neutral Density (ND) filters. Ranging from a transmission of 0.001 to 0.5.
12. Atomic force microscope (Digital Instruments).

4 Results

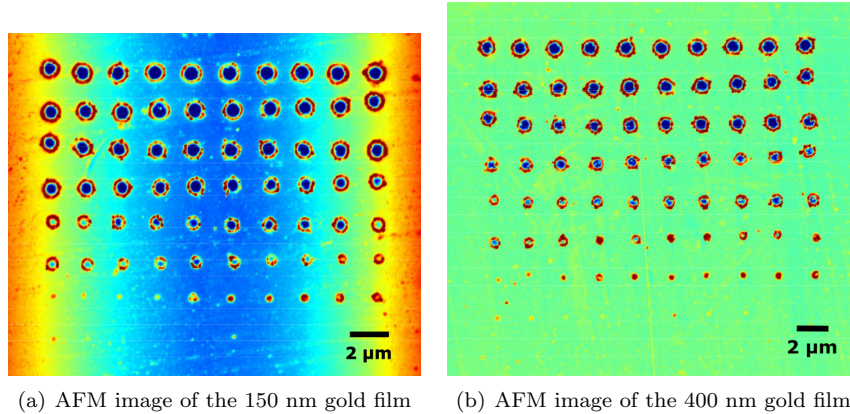


Figure 4.1: AFM images for ablation experiments

The first part that we address is the energy deposition which is simulated by the FDTD method, accessible in the experiment by examining the self reflectivity. By measuring the self reflectivity, we get a better grasp how much energy has been deposited in the material. Bear in mind, the energy not reflected by the material does not need to be absorbed completely as there is also the possibility of scattering on the induced plasma.

The second part we will address is the actual ablation of the holes. By studying the geometry of the holes, we can try to understand how the energy has moved through the material. In this report we will focus on the depth and the width, including the case of overlapping holes.

Finally, it is useful to keep in mind that an important application of making such hole arrays is the guidance of light. Transmission spectroscopy is a very important method to study the usability of these holes as wave guides. Spectroscopy has not been applied yet for this report, but the method has been tested with a combination of a white light laser and an AOTF. More about this experiment can be found in section 5.

4.1 Self reflectivity

First, we examine the self reflectivity. The energy of each laser pulse is measured and calibrated with a photo diode. Furthermore, the reflection of the sample is observed and measured by the CCD camera. For low intensities, below ablation threshold, the reflectivity of gold is 0.975 and is used for calibration. In our experiment ablation has been performed on 150 nm and 400 nm gold films

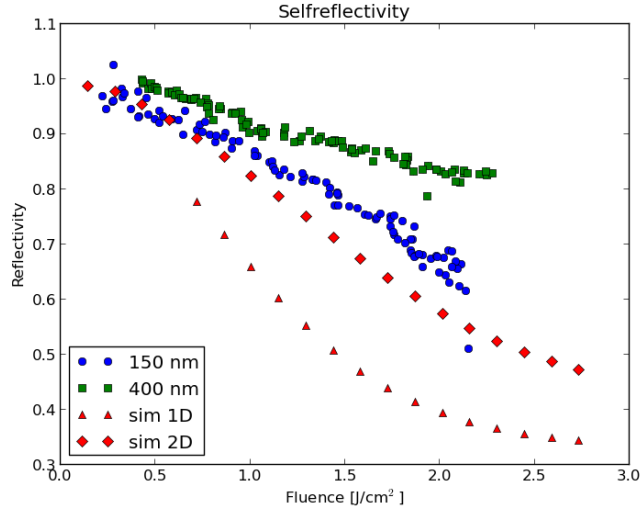


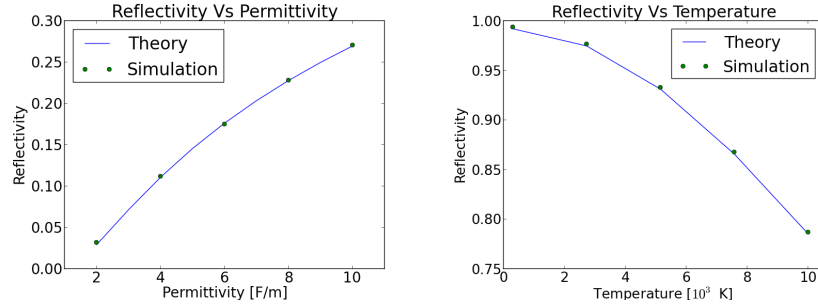
Figure 4.2: Self reflectivity of single shot experiments and simulations as a function of the fluence. The light pulses are 126 fs long and have a wavelength of 800 nm. The experiments have been performed on gold films of 150 nm (blue circles) and 400 nm (green squares). In the simulations a 400 nm film is used, both for 1D (red triangles) and 2D (red diamonds).

(see figure 4.2). With increasing fluence both films show a steady decrease in reflectivity.

For the simulations we calculated the reflectivity by running the model twice, once with the metal film in place and once just in air. By subtracting the results we obtain the calculated reflected fields. This can then be divided by the fields in the air run, which gives you the reflectivity (see figure 4.2). When we examine the results we find a significant difference in the 1D and 2D simulation. This is expected from the fact that for 1D we determine the reflectivity at the center of the pulse. Here, the fluence on the surface is highest, which causes a larger change in the metallic properties and resulting in a lower reflectivity. We can conclude that the 1D simulation is not realistic and will therefore not be mentioned in the morphology section.

In the 2D case, we account for the entire width of the pulse where at the edges the fluence is much smaller. This causes a smaller change on the reflectivity, resulting in overall higher reflectivity over the whole width. Of course, this is a more realistic comparison to our experiment.

The 2D simulation is partly in good agreement with the experiments. However, where the experiment has a linear dependency on the fluence, the simulation shows a dip in the self reflectivity. We note that the FDTD was calibrated with vanishing fluences and compared with theoretical reflectivity (see figure



(a) Reflectivity as a function of permittivity of the material. (b) Reflectivity as a function of temperature of the material.

Figure 4.3: Reflection simulations where the pulses do not interact with the material.

4.3). One can see that the simulations faithfully match the theory, suggesting that our FDTD works and that deviations of the calculated results with the experiments is most likely due to too simple assumptions about the interaction process.

It could be that diffusion does play a significant part during the deposition of the laser energy. For low fluences the difference is hardly noticeable, but for larger fluences the build-up of heat of the electrons, due to the lack of diffusion, could account for an overestimate in the change of self reflectivity. If diffusion is taken in account the heat of the electrons would be diffused into the material, causing lower temperatures and thus less of change in the self reflectivity.

Another option could be that the absorbed energy is not completely used for heating. The conversion from intensity to temperature (see equation 2.60) is then too high and only a fraction of the intensity should be converted.

4.2 Morphology

We will now address the geometry of the holes, in particular the depth of the holes. For this we need to discuss the different criteria for our simulations and decide which ones are the most appropriate. Four criteria have been compared which each other: first we have evaporation (see equation 2.66) and melting, where with the latter the lattice temperature exceeds the melting temperature of gold. Second, we examined how defining a minimum electron temperature as a criterion for ablation compares to evaporation and melting (see figure 4.4). We find that the depths with criteria for criteria with an high and low electron temperature is largely the same for evaporation and melting depths, respectively. The first observation follows from the evaporation equation (see equation 2.66) as for larger fluences the electron temperature is much higher than the lattice temperature and is therefore dominant.

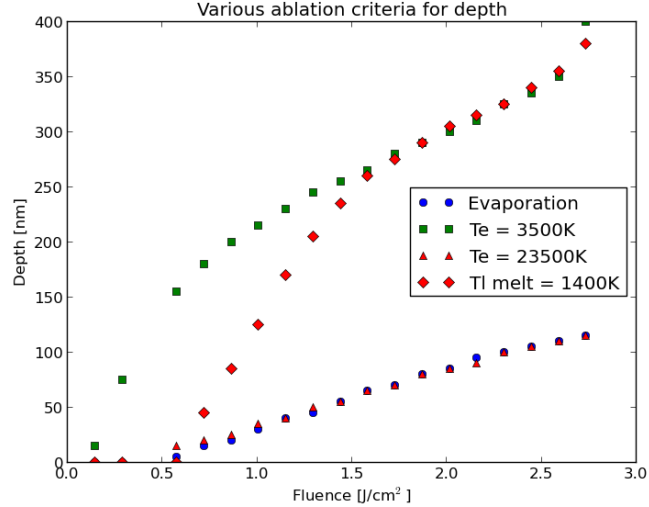


Figure 4.4: Depth measurements by simulations as a function of the fluence for different ablation criteria: evaporation (blue circles), low electron temperatures (green squares), high electron temperatures (red triangles) and the lattice at melting temperature (red diamonds).

The depths with melting and low electron temperature criteria become similar starting at a depth of 250 nm. This could be explained that in our simulations from this point electrons are solely heated due to the diffusion and not by deposition of the laser energy as well. The temperature differences become smaller, causing the heat conductivities to become constant. This means that heat diffuses through the material with a constant speed, which explains why the ablation depth goes linear with fluence when diffusion is the only active energy transport. Before the 250 nm point the electrons are heated during the energy deposition to such a level that without diffusion it would already heat the atoms enough for ablation. This causes the change in depth between the scenario's with the two different criteria.

When looking at the experiments, we see that for the threshold for both depths ablation is around 1.1 J/cm^2 (see 4.5; 150 nm: blue circles, 400 nm: green squares). Both films show a linear increase in depth with increasing fluence, which is caused by diffusion. One can see that the ablation threshold of the simulation with the melting and low electron temperature criterion is much too low. Furthermore, the slopes with these two criteria are much too flat slope compared to the experiments. The melting temperature seems to be the best option from the four as the shape and slope is quite similar to the experiments. However, it still has a low threshold (0.5 J/cm^2) to 1.1 J/cm^2 for the 150 and 400 nm film in the experiments (red diamonds). However, the difference with the experiments is consistent with the reflectivity. Lower reflectivity means

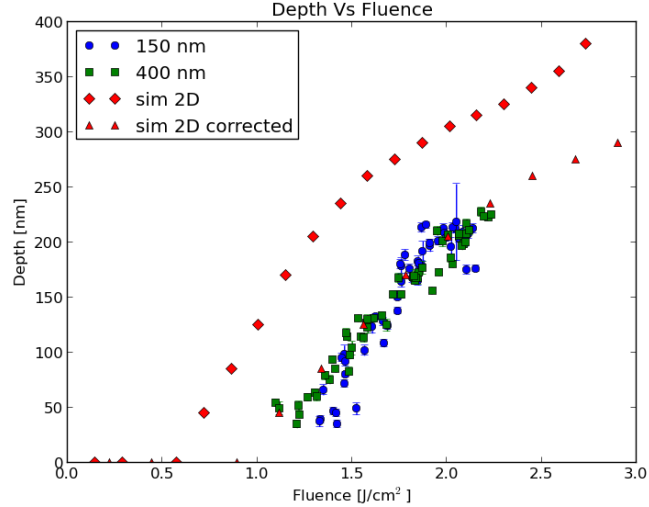


Figure 4.5: Depth measurements by an AFM of single shot experiments and simulations as a function of the fluence. The light pulses are 126 fs long and have a wavelength of 800 nm. The experiments have been performed on gold films of 150 nm (blue circles) and 400 nm (green squares). In the simulations a 400 nm film is used, both for 1D (red triangles) and 2D (red diamonds).

that more energy is absorbed, causing a lower threshold for the same fluence. In fact, when correcting the results of the model with a factor of roughly 1.6 to the fluence, we find that the simulations with a melting criterion fits the experiments quite well (red triangles). This indicates that we might oversimplified or ignored a significant process. Before we go deeper into these possibilities, we first will look at the diameter of the holes.

The next geometry parameter we will discuss is the diameter of holes. First, we will again compare the simulation results for different criteria (see figure 4.6). Again, the evaporation and high electron temperature criteria virtually coincide, though widths for the the electron temperature criterion has a small positive offset. It is notable that the melting temperature criteria follows the same behaviour, where with the depth its slope was much steeper. This can be explained if the temperature of the lattice increases faster in depth than in width. As diffusion of the lattice temperature was neglected the heating of the lattice can only be caused by electron diffusion and subsequently the coupling between electrons and phonons. This would mean that the heat of the electrons would diffuse faster in depth than in width which can be explained by the fact that at the surface the surroundings are heated as well, causing the largest gradient to be into the material.

If we compare the simulations with the experiments it is not surprising that the simulation already has a width at a lower threshold as this was the case with

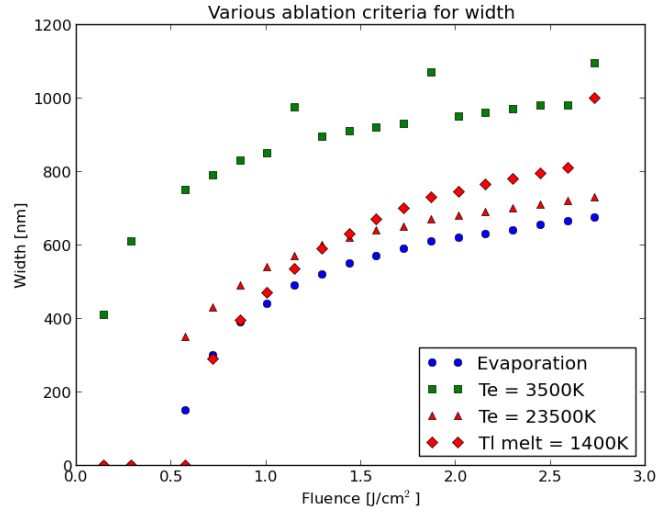


Figure 4.6: Diameter measurements by simulations as a function of the fluence for different ablation criteria: evaporation (blue circles), low electron temperatures (green squares), high electron temperatures (red triangles) and the lattice at melting temperature (red diamonds).

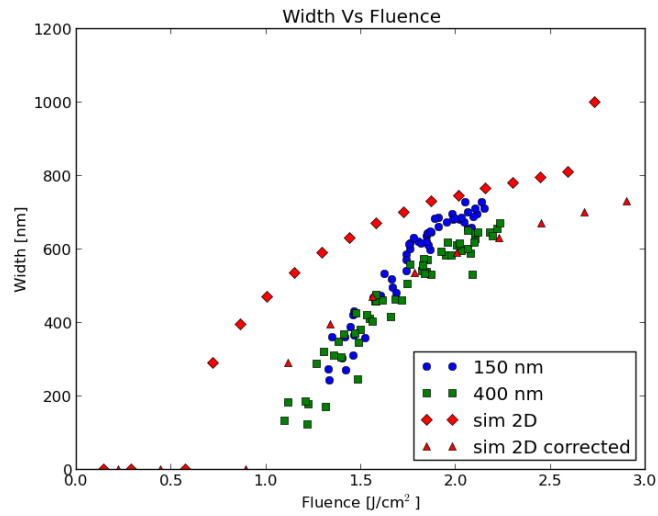


Figure 4.7: Diameter measurements by an AFM of single shot experiments and simulations as a function of the fluence. The light pulses are 126 fs long and have a wavelength of 800 nm. The experiments have been performed on gold films of 150 nm (blue circles) and 400 nm (green squares). In the 2D simulations (red diamonds) a 400 nm film is used.

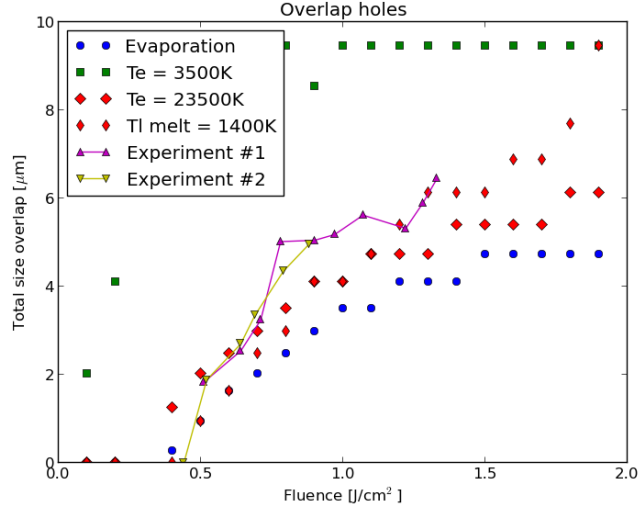


Figure 4.8: Overlap by an AFM of single shot experiments and simulations as a function of the fluence. The light pulses are 126 fs long and have a wavelength of 800 nm. The experiments have been performed twice (triangles up and down) on gold films of 150 nm for a number of fluences. In the 2D simulations a 400 nm film is used and we compare the experiment to the criteria discussed in figure 4.6

the depth (see figure 4.7). However, like in the simulations we see for the 400 nm film that the slope is gradually become shallower which we did not see with the depth. This could mean that diffusion has indeed a preference to go deeper.

Like with the depths of the holes, the simulation are off with a factor of roughly 1.6. When corrected, the results fit quite nicely with the experiments, strengthening our assumption that we neglected a significant process. In the self reflectivity section (section 4.1) we already discussed the possibility of the neglected diffusion during deposition and the intensity-absorption ratio. Both processes could explain the factor we found examining the depths and widths. Both reduces the maximum temperature the material has at every given location, causing the ablation threshold to become higher.

Finally, we will look at another experiment we did, where we studied the overlap between individual holes on the 150 nm film. For this experiment we ablated a line of holes where the intermediate distance decreases linearly from 1 μm to 0.02 μm in 20 equal steps (see appendix F for the AFM images and profiles). We did this routine for a number of fluences. The criteria for overlap was if the rims of the holes would cross each other. We then measure the size of the crater consisting of all the overlapping holes.

When we look at the results (see figure 4.8), we can see that the model follow the experimental results quite well. This is quite strange as the ablation threshold

suddenly is 0.5 J/cm^2 while before this was much higher (1.1 J/cm^2).

It should be noted that in retrospect the accuracy at which the stages move is too low for this experiment. To distinguish overlap we need to be able to accurately move the stage less than $1 \mu\text{m}$, while the accuracy of the stage is only $4 \mu\text{m}$. One could already see in figure 4.1 that the holes are roughly aligned but can differ from their supposed position with a too high uncertainty. This means that the results in figure 4.8 are not reliable and cannot be used to draw conclusions from.

5 Transmission spectroscopy

In our setup we have the option to perform transmission spectroscopy with the beam of a white light femtosecond laser. The white light laser is used in combination with a so-called Acoustic Optical Tunable Filter (AOTF) to filter specific wavelengths for the spectroscopy, while keeping the beam profile and direction constant. The reason a narrow bandwidth is used is not only to enhance the spectral resolution, but is also required to reduce the power of the probe beam and prevent damaging of the sample.

The special advantage of an AOTF to filter the light is that an AOTF works electronically and can therefore scan much faster than a mechanical device (e.g. a diffracting prism). The high-speed performance allows for a quick measurement of the transmission over the entire spectrum and reduces fluctuations of the setup as much as possible.

5.1 Theory

An AOTF uses travelling sound waves in a crystal to create changes in refractive index (in the order of 10^{-8} to 10^{-5}). Incoming photons will interact with these perturbations and diffract accordingly. In order to properly describe the effect light will be described in wave vectors,

$$|k| = \frac{\omega n}{c} \text{ (photons)} \quad (5.1)$$

$$|k| = \frac{2\pi f}{V_a} \text{ (phonons)} \quad (5.2)$$

Here, ω is the frequency of the light, n the refractive index of the medium, c the speed of light, f the frequency of the sound wave and V_a the speed of the sound wave. Interacting fields have to apply to the k -matching condition ^[15],

$$\vec{k}_i + \vec{k}_a = \vec{k}_d \quad (5.3)$$

Since the light frequency is virtually constant as the sound waves have a much smaller frequency, the wave vector will be constant. In a wave vector diagram the wave vectors are indicated with vector arrows and one can easily see that an incoming wave vector can only point from the origin to a semicircle, also called the dispersion surface (see figure 5.9). This surface represents the wave vector light will have when encountering a certain refractive index. The same restriction goes for the out coming, diffracted wave vector. Thus, wave vectors have to apply to both the k -matching condition as the dispersion restriction.

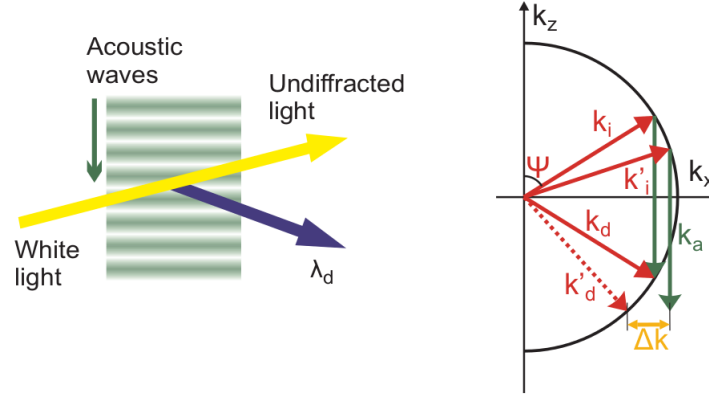


Figure 5.9: (Left) Principle of acousto-optic filtering: light is diffracted by a moving diffraction grating that is generated with acoustic perturbations. (Right) Interaction of acoustic waves with optical waves in wave vector space. The black circle is a dispersion surface for light of a particular wavelength. If light is incident under an angle Ψ , the incoming wave vector (k_i) couples to the diffracted wave vector (k_d) due to interaction (addition) with the acoustic wave vector (k_a). A momentum mismatch (Δk) occurs if light is incident under an angle other than Ψ .^[16]

This means that only a specific k_a can cause a diffracted k_d . Other wave vectors would cause a mismatch Δk and therefore no diffraction occurs.

Moreover, the crystal in an AOTF is birefringent causing another effect. The speed of photons in birefringent materials depends on the polarization of the light, due to the anisotropy (directional dependence) of the material. Anisotropy can be caused by the manner in which molecules are lined up or by the construction of the crystal lattice. In uni-axial materials there is a single anisotropy axis, causing ordinary and extra-ordinary rays: polarizations perpendicular and parallel to the anisotropy axis, respectively. Extra-ordinary rays encounter a larger refractive index (thus an shorter wave vector) along the axis of anisotropy, causing an elliptical dispersion surface (see figure 5.10).

The wave vector of the sound wave can cause the polarization of the incoming light to change from ordinary to extra-ordinary. As the wave vector difference between polarizations is different per wavelength, one can tune the out coming wavelength by tuning the frequency of the sound wave while keeping the same beam direction and profile. Moreover, the polarization of the out coming wave vector will be extra-ordinary.

5.2 Setup

List 5.1: Items used in the ablation setup

1. White light laser, NKT Photonics SuperK Extreme EXR-4

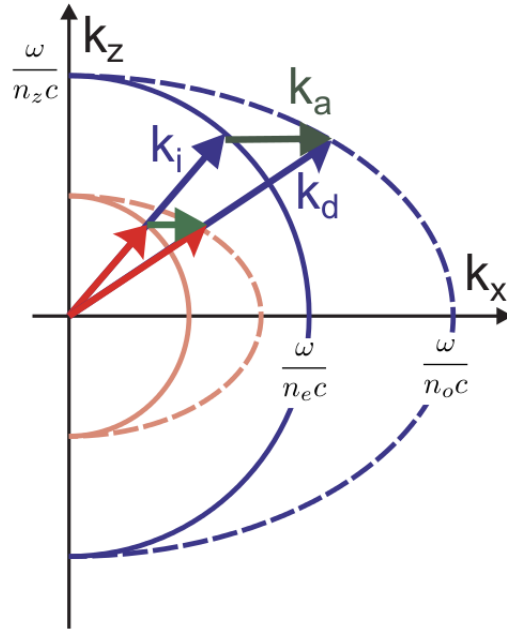


Figure 5.10: Wave vector diagrams for interaction of light and acoustics in a birefringent medium. Wave vectors and dispersion curves for blue light (large blue arrows and circle) and red light (small red arrows and circle) are shown. Since the medium is anisotropic ($n_o < n_e$) ordinary polarized light (solid curves) and extra-ordinary polarized light (dashed curves, ellipsoidal) have different dispersion curves; light polarized parallel to the axis of anisotropy (\hat{z}) encounters a larger refractive index, and therefore, a smaller wave vector. Incident light (k_i) interacts with an acoustic wave (k_a , green arrow) upon a polarization rotation and diffracts into k_d . K-vector matching for blue light requires a different length of the acoustic wave vector than for red light.^[16]

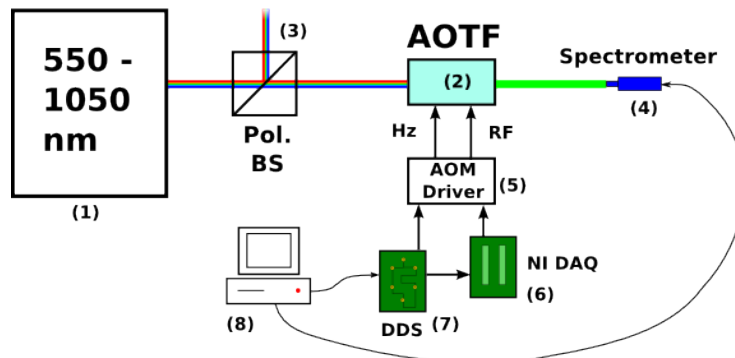


Figure 5.11: Schematic view of the AOTF calibration setup

2. Polarizing beam splitter.
3. AOTF crystal, Crystal Technology (PCAOM NIR 1). Acoustic frequency range: 48-86 MHz, Wavelength range: 640-1100 nm.
4. Spectrometer, Ocean Optics (HR2000CG UV-NIR). Connected to a 200 μm fiber (UV-VIS High OH content, 300-1100 nm) for analysis of the laser spectrum.
5. Neutral Density (ND) filters. Ranging from a transmission of 0.001 to 0.5.
6. DNS board, National Instruments.
7. NIDAQ board, National Instruments.

In the setup for the AOTF calibration experiment (see figure 5.11) the white light laser is first send through a polarizing beam splitter to polarize the light. The beam then traverses to the AOTF where a diffraction pattern is created (see section 5.1) where the 1st order is send straight through, while the 0th is deflected with an angle to a beam dump. Normally, this is the other way around but the crystal is cut in such a fashion that the 0th is refracted under an angle. The first-order beam is then send to the sample for analysis. The AOTF is powered by the AOM driver, which provides an RF power at the desired acoustic frequency. The driver is connected to a DNS board for computer automated control and a NIDAQ board to create a delay for the RF power. The purpose of the delay is explained in section 5.3.

5.3 Results

As discussed before, the advantage of using an AOTF for wavelength specific transmission spectroscopy is the speed at which it can sweep through a spectrum. We have to make sure that the wavelengths are indeed selected by the AOTF at the time we believe it to be. For this we first check which wavelength corresponds to which frequency of the sound wave in the AOTF. This is done by measuring the spectrum of the laser for a range of different AOTF frequencies. From the manufacturer we know that the relation between the AOTF frequency and the outgoing wavelength is a 4th degree polynomial which we can use as a gauge (see figure 5.12).

We now know when we send a known frequency at a given time to the AOTF what wavelength should be emitted at that time. In order to check this we will do an sweep through the spectrum by rapidly changing the AOTF driver frequency but will feed the AOTF only a short pulse of RF power after a specified delay (see figure 5.13). This means that for a certain delay only a narrow range of wavelengths will be sent from the AOTF (the wavelengths on the blue line within the green pulse). We then analyse the out coming light with a spectrometer (see figure 5.14). Our prediction corresponds very well with our measured data which indicates that the AOTF is working as we thought it would.

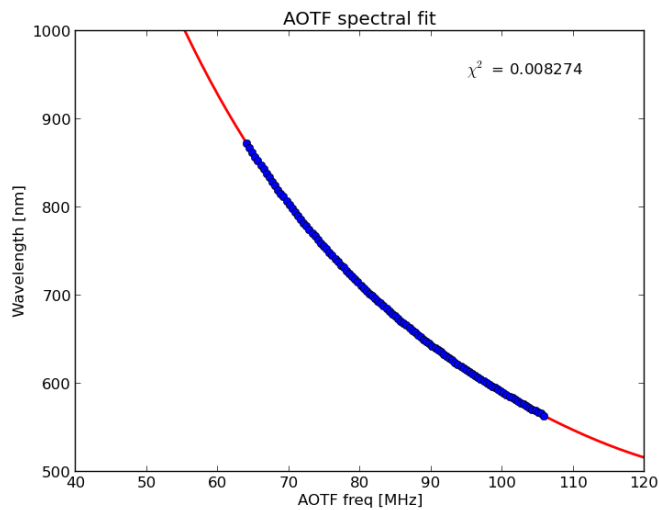


Figure 5.12: Spectra for different AOTF frequencies. The blue points are the measured wavelengths for each AOTF frequency, the red line is the fit with a goodness of $\chi^2 = 0.008274$

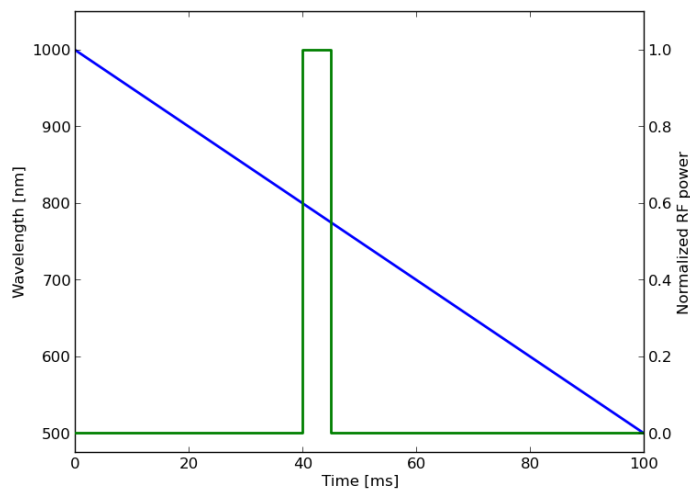


Figure 5.13: Sketch of sending a peak pulse of RF power for a known delay. While sweeping through the spectrum over time (blue line), the AOTF only gets a RF power after a certain delay (green) resulting in only a small range of wavelengths being emitted.

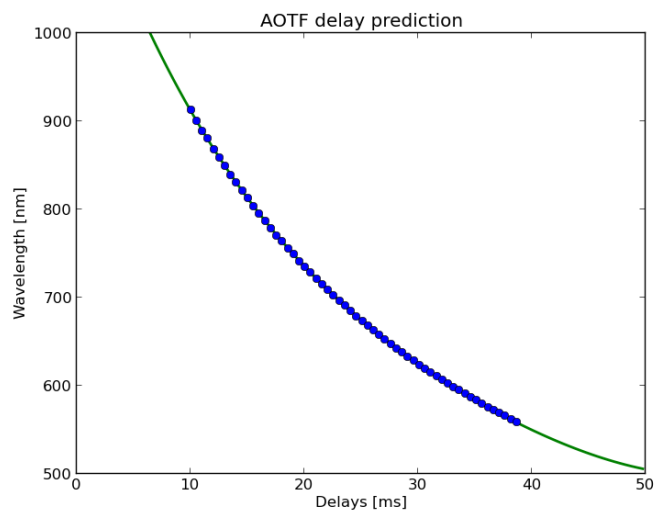


Figure 5.14: Wavelength emitted after a certain time. The blue points are the wavelengths measured after a known delay. The red line is the prediction as we know which frequencies (converted to wavelengths with relation from figure 5.12) corresponds to which delay.

Unfortunately, we were yet not able to create suitable samples with laser ablation to check the optical transmission of these samples with the present setup.

6 Conclusion

In this report we discussed the energy deposition and spread of femtosecond laser ablation on thin gold films. Our main question was how the dynamics of femtosecond ablation on thin gold films can be accurately described. Our hypothesis was that the two-temperature model could be a likely candidate. We compared the model with the experimental results on two different aspects of the process, self reflectivity and the geometry of the ablated holes.

When we look at the self reflectivity we see that the model is in rather good agreement with the experiments. It shows the same descent in self reflectivity within a range of fluences, though it descends a bit too fast for large fluences. This can be explained by the sharp separation of the heat diffusion, causing too high of a build-up of heat during the energy deposition and thus an overestimate of the drop in self reflectivity.

This small mismatch has of course its effect on the geometry of the ablated holes. The fluence threshold in the model is much lower than in the experiments, however the order of magnitude in depth and the rate of ablation is quite similar. The model is actually off with a factor of around 1.6, suggesting that we missed or simplified a significant process. The lack of diffusion during the energy deposition could be an explanation, but it can also be that we overestimate the transfer between the intensity of the electric fields and the absorbed energy. It is certainly worth while to have a closer look at the effects of these processes.

A different study of femtosecond ablation is the suitability of the holes as a light wave guide. Transmission spectroscopy is an important tool to establish this and therefore we studied the possibility of using a white light laser with an AOTF. It shows that an AOTF is very suitable for switching between wavelengths in a very short time frame (μs). This feature is rather useful to diminish the variation in pulse energy of the laser.

7 Dankwoord

Ze zeggen wel eens dat je scriptie het intensiefste is wat je tijdens je studie zal doen. Bij mij was dit geen uitzondering en over de periode van een jaar heeft het een groot deel van mijn tijd en aandacht opgeslokt. Zoals in elk onderzoek waren er pieken en dalen, zowel wetenschappelijk als mentaal. Hoewel het soms wel anders lijkt als je in je eentje in een donker lab werkt, hoef je het gelukkig niet helemaal alleen te doen. De personen die hun spreekwoordelijke steentje hebben bijgedragen wil ik daarom hier speciaal bedanken.

First, I would like to thank Hao Zhang, my PhD supervisor who not only explained me the comprehensive setup but who was also an incredible help with the creation of my FDTD simulations. I know for sure it would have taken me much longer without his help.

Daarnaast is er een groep mensen met wie ik het afgelopen jaar misschien meer contact heb gehad dan me soms lief was, maar die wel een ontzettende steun zijn geweest. Uiteraard heb ik het hier over de bewoners van kamer OL254: Bas, Bruno, Christiaan, Sebastiaan, Tessa en Zimma. Behalve het feit dat we altijd bereid waren elkaar te helpen als iemand er even niet uit kwam, was de kamer ook een bron van gezelligheid en soms broodnodige afleiding. Het afgelopen jaar zijn er vele mooie anekdotes and uitspraken uit die kamer gekomen, die ik niet snel zal vergeten. Hoewel die uiteraard niet in mijn verslag zijn opgenomen ('What happens in OL254 stays in OL254') zullen die verhalen voor mij onlosmakelijk met mijn onderzoek verbonden zijn.

Tenslotte wil ik graag mijn begeleiders bedanken die me gedurende het jaar veel hebben gelopen. Jaap Dijkhuis, die de grote lijnen van mijn onderzoek in de gaten hield en zeker tegen het einde ontzettende nuttige input leverde op mijn analyses. Denise Krol, die ik al kende via mijn stage in Amerika en mij veel heeft geholpen om het grotere plaatje achter mijn onderzoek goed te begrijpen en dat ook op een duidelijke, heldere manier kan uitleggen, en tenslotte Dries van Oosten. Neil Troy, die mijn begeleider in Amerika was en ook 3 maanden in onze groep heeft gewerkt, noemde Dries 'the smartest man he has ever met' en na een jaar dat zelf te hebben kunnen ervaren, sluit ik me daar graag bij aan. Ik heb ontzettend veel diverse en nieuwe dingen van hem geleerd, die niet eens per se over de natuurkunde hoefde te gaan.

Er rest mij nu alleen nog maar te zeggen: Bedankt!

8 Appendix

A Laser fluence

When dealing with the laser pulse as a simple intensity profile, the laser pulse is described by:

$$S(z, t) = I_0(1 - R)L_p^{-1}\exp(-z/L_p)\exp(-(t - t_0)^2/2\sigma^2)\exp(-2(r - r_0)^2/r_L) \quad (\text{A.1})$$

The term consists of the peak intensity I_0 , dependent on the laser fluence F and pulse duration τ_L by $I_0 = F/\tau_L(\sqrt{\pi/4\ln(2)})$. This intensity is absorbed, scattered or transmitted to a skindepth L_p . The skindepth also specifies the logarithmic decay in the z-direction. The third term is describing the Gaussian time-dependence profile of the laser input with pulse duration τ_L (Full Width at Half-Maximum(FWHM)) resulting in $\sigma = \tau_L/\sqrt{8\ln(2)}$. Finally, the last term described the Gaussian radial profile of the laser with a pulse width of r_L .

To find an expression for the fluence F as function of the intensity $I(t)$, we integrate the intensity (which is a gaussian) over time. When we integrate over time using the the FWHM pulse duration τ_L (see equation A.2) and integrate over space using the general gaussian expression (see equation A.3) we can also find the expression for σ as described in equation A.1.

$$\begin{aligned} F &= \int I(t)dt \\ F &= \int I_0 \exp(-\log 2 \frac{t^2}{(\frac{1}{2}\tau_L)^2}) dt \quad (\text{A.2}) \\ F &= \sqrt{\frac{\pi}{4\log 2}} \tau_L I_0 \end{aligned}$$

$$\begin{aligned} F &= \int I(t)dt \\ F &= \int I_0 \exp(\frac{-t^2}{2\sigma^2}) dt \quad (\text{A.3}) \\ F &= \sqrt{2\pi}\sigma I_0 \end{aligned}$$

$$\sigma = \frac{\tau_L}{\sqrt{8\log 2}} \quad (\text{A.4})$$

B FDTD

B.1 Residual integration

$$\chi(t) = \frac{1}{2\pi} \int_{-\infty}^{\infty} d\omega \chi(\omega) e^{i\omega t} \quad (\text{B.1})$$

$$\chi(t) = \frac{-\omega_p^2}{2\pi} \int_{-\infty}^{\infty} d\omega \frac{e^{i\omega t}}{\omega(\omega - i\gamma)} \quad (\text{B.2})$$

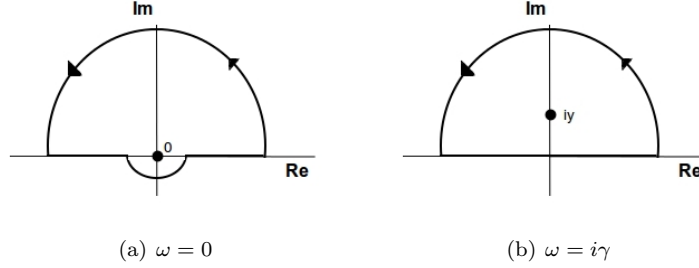


Figure B.1: Contour integration around the two poles $\omega = 0$ (a) and $\omega = i\gamma$ (b)

This integral can be solved by the residue theorem, where there are two poles: $\omega = 0$ and $\omega = i\gamma$ (see also figure B.1).

$$\chi(t) = \frac{-\omega_p^2}{2\pi} 2\pi i \operatorname{Res} \left[\frac{e^{i\omega t}}{\omega(\omega - i\gamma)} \right] \quad (\text{B.3})$$

$$\chi(t) = \frac{-\omega_p^2}{2\pi} 2\pi i \left[\frac{e^{i\omega t}}{\omega - i\gamma} \Big|_{\omega=0} + \frac{e^{i\omega t}}{\omega} \Big|_{\omega=i\gamma} \right] \quad (\text{B.4})$$

$$\chi(t) = \frac{\omega_p^2}{\gamma} [1 - e^{-\gamma t}] u(t) \quad (\text{B.5})$$

Mind the $u(t)$ at the end of $\chi(t)$. This is the block function, which is 0 for $t < 0$ and 1 for $t \geq 0$, and is used to define $t = 0$ as the beginning of the simulation as it is assumed that there are no functions before.

B.2 I and S

$$\vec{D}(t) = \epsilon_\infty \vec{E}(t) + \vec{I}(t) + \vec{S}(t) \quad (\text{B.6})$$

$$\vec{I}(t) = \frac{\sigma}{\epsilon_0} u(t) * \vec{E}(t) \quad (\text{B.7})$$

$$I(t) = \frac{\sigma}{\epsilon_0} \int_0^t E(t') \cdot dt' \quad (\text{B.8})$$

$$I^n = \frac{\sigma \cdot \Delta t}{\epsilon_0} \sum_{i=0}^n E^i \quad (\text{B.9})$$

$$= \frac{\sigma \cdot \Delta t}{\epsilon_0} E^n + \sum_{i=0}^{n-1} E^i \quad (\text{B.10})$$

$$= \frac{\sigma \cdot \Delta t}{\epsilon_0} E^n + \frac{\sigma \cdot \Delta t}{\epsilon_0} E^{n-1} \quad (\text{B.11})$$

$$= \frac{\sigma \cdot \Delta t}{\epsilon_0} E^n + I^{n-1} \quad (\text{B.12})$$

The integral has a lower boundary of 0 due to the block function. When discretized we can express the term in E^n and its previous value I^{n-1} . This will become useful in a moment, but first the S -term needs to be converted.

$$S(t) = \chi_1 \cdot \gamma e^{-\gamma t} u(t) * \vec{E}(t) \quad (\text{B.13})$$

$$S(t) = \chi_1 \cdot \gamma \int_0^t e^{-\gamma(t-t')} E(t') \cdot dt' \quad (\text{B.14})$$

$$S^n = \chi_1 \cdot \gamma \Delta t \sum_{i=0}^n e^{-\Delta t \gamma (n-i)} E^i \quad (\text{B.15})$$

$$S^n = \chi_1 \cdot \gamma \Delta t \left[E^n + \sum_{i=0}^{n-1} e^{-\Delta t \gamma (n-i)} E^i \right] \quad (\text{B.16})$$

Here $u(t)$ again causes the lower boundary of 0. When discretized E^n is split off again, leaving a sum notation from 0 tot $n - 1$. The discretized function S^n can also be filled in for $n - 1$, replacing n with $n - 1$ in equation B.15.

$$S^{n-1} = \chi_1 \cdot \gamma \Delta t \sum_{i=0}^{n-1} e^{-\Delta t \gamma (n-1-i)} E^i \quad (\text{B.17})$$

$$S^{n-1} = \chi_1 \cdot \gamma \Delta t e^{\gamma \Delta t} \sum_{i=0}^{n-1} e^{-\Delta t \gamma (n-i)} E^i \quad (\text{B.18})$$

$$(\text{B.19})$$

Equation B.18 can be used to express S^n in terms of its previous value S^{n-1} in equation B.16.

$$S^n = \chi_1 \cdot \gamma \Delta t E^n + e^{-\gamma \Delta t} S^{n-1} \quad (\text{B.20})$$

Now all the terms from equation 2.15 are known in discretized form and can be filled in,

$$D^n = \epsilon_r E^n + I^n + S^n \quad (\text{B.21})$$

$$D^n = \epsilon_r^* E^n + \frac{\sigma \cdot \Delta t}{\epsilon_0} E^n + I^{n-1} + \chi_1 \cdot \gamma \Delta t E^n + e^{\gamma \Delta t} S^{n-1} \quad (\text{B.22})$$

C Damping collisions

At low temperature (but still above the Debye temperature) the electron-phonon collision dominates whereas at high temperature (but below the Fermi temperature) the electron-electron collisions dominate^[14]. The first can be described by:

$$\frac{1}{\tau_{e-e}} = \frac{1}{3} v_F^2 C_e W_{e-e} = AT^2 \quad (\text{C.1})$$

where v_F is the Fermi velocity, C_e the heat capacity and W_{e-e} is the thermal resistivity. The electron-phonon collision frequency can be described by:

$$\frac{1}{\tau_{e-ph}} = \frac{\rho(T) n_e e^2}{m} = BT \quad (\text{C.2})$$

where ρ is the electronic resistivity, n_e the electron density, e the electron charge and m the effective electron mass. Constants A and B can be found in table 2.1^[14].

D Dielectric constant

The motion of an electron can be described by applying Newton's law, resulting in the following motion equation:

$$m_e \ddot{r} = -eE(t) - \gamma m_e \dot{r} \quad (\text{D.1})$$

Here, the general force (m_e is the electron mass) consist of the electric force (e is the charge of the electron and $E(t)$ the electric field) and the damping force (γ is the damping constant). To solve this equation, we need a sample solution and a description of $E(t)$ which generally are both given in the form of:

$$r(t) = r_0 e^{i\omega t} \quad (\text{D.2})$$

$$E(t) = E_0 e^{i\omega t} \quad (\text{D.3})$$

Note that many physicists use the alternative form $e^{-i\omega t}$. In this thesis the 'engineering' method is used with a positive sign. Filling in the sample solution and $E(t)$ gives you the motion of the electron. This can be than used to calculate the polarization P .

$$r(\omega, t) = \frac{e}{m_e} \frac{1}{\omega^2 - i\omega\gamma} E_0 e^{i\omega t} \quad (\text{D.4})$$

$$P(t) = -Ner(t) \quad (\text{D.5})$$

$$P(\omega, t) = -\frac{Ne^2}{m_e} \frac{1}{\omega^2 - i\omega\gamma} E_0 e^{i\omega t} \quad (\text{D.6})$$

The polarization can also be given by the electric field (E) and the electrical susceptibility (χ).

$$P(t) = \epsilon_0 \chi E(t) \quad (\text{D.7})$$

$$\chi(\omega) = \frac{P(\omega, t)}{\epsilon_0 E(t)} \quad (\text{D.8})$$

$$\chi(\omega) = -\frac{Ne^2}{\epsilon_0 m_e} \frac{1}{\omega^2 - i\gamma\omega} \quad (\text{D.9})$$

$$\chi(\omega) = -\frac{\omega_p^2}{\omega^2 - i\gamma\omega} \quad (\text{D.10})$$

χ is now given in the frequency domain and can be converted to the time domain with Fourier transform.

In some cases the dielectric constant also consists of a Lorentz term, expanding the equation to:

$$\epsilon_r^* = \epsilon_\infty - \frac{\omega_p^2}{\omega^2 - i\omega\gamma} + \frac{\omega_{p0}^2}{\omega_0^2 - \omega^2 - i\gamma_0\omega} \quad (\text{D.11})$$

The parameters are dependent on the material and can be found in table 2.1. The parameters are fitted with experimental data and are based on the Drude-Sommerfeld theory combined with interband transitions ^[17].

The dielectric constant can also be described by:

$$\begin{aligned} \epsilon_D &= (n_R + in_I)^2 & (\text{D.12}) \\ \epsilon_D &= n_R^2 - n_I^2 + i 2n_R n_I \end{aligned}$$

If we equalize the real part of ϵ_D to $n_R^2 - n_I^2$ and the imaginary part to $2n_R n_I$, we can find an expression for n_R and n_I .

$$n_R = \sqrt{\frac{\alpha + \sqrt{\alpha^2 + \beta^2}}{2}} \quad (\text{D.13})$$

$$n_I = \frac{\beta}{\sqrt{2(\alpha + \sqrt{\alpha^2 + \beta^2})}} \quad (\text{D.14})$$

Now, we can use these parts of the refractive index to calculate the reflectivity R and skindepth L_p .

However, there are also non-linear processes to consider. The extra term can be described by (citaat!):

$$\epsilon_2 = \frac{3}{4}\chi^{(3)}E^2 \quad (\text{D.15})$$

$$E = \sqrt{\frac{2I}{n\epsilon_0 c}} \quad (\text{D.16})$$

Here, $\chi^{(3)}$ is the non-linear coefficient and E the electric field inside the material. E is related to the intensity of the pulse I , the refractive index (assuming just ϵ_1) and the speed of light c .

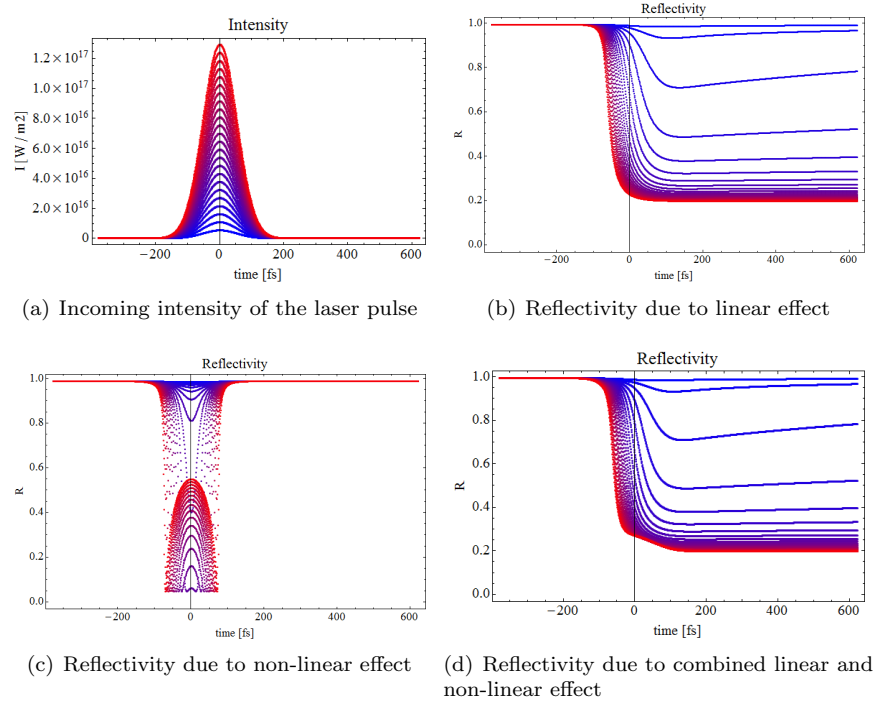


Figure D.0: Non-linearity in reflectivity

E Diffusion

$$C_e(T_e) \frac{\partial T_e}{\partial t} \equiv \nabla \cdot (K_e(T_e) \nabla T_e) \quad (\text{E.1})$$

$$\begin{aligned} T^{n+1} &= T^n + \frac{\Delta t}{C_e(T_e)} (\nabla \cdot (K_e(T^n) \nabla T^n)) \\ &= T^n + \frac{\Delta t}{C_e(T_e)} D(T^n) \end{aligned} \quad (\text{E.2})$$

1D

$$D(T) = \frac{\partial}{\partial z} (Ke(T) \frac{\partial}{\partial z} T) \quad (E.3)$$

$$\begin{aligned} D(T_i) &= \frac{1}{\Delta z} \left[(Ke(T) \frac{\partial}{\partial z} T)_{i+\frac{1}{2}} - (Ke(T) \frac{\partial}{\partial z} T)_{i-\frac{1}{2}} \right] \\ &= \frac{1}{\Delta z} \left[(Ke(T)_{i+\frac{1}{2}} \frac{1}{\Delta z} (T_{i+1} - T_i)) - (Ke(T)_{i-\frac{1}{2}} \frac{1}{\Delta z} (T_i - T_{i-1})) \right] \\ &= \frac{1}{\Delta z^2} \left[\frac{Ke(T)_{i+1} + Ke(T)_i}{2} (T_{i+1} - T_i) + \right. \\ &\quad \left. \frac{Ke(T)_{i-1} + Ke(T)_i}{2} (T_{i-1} - T_i) \right] \end{aligned} \quad (E.4)$$

2D

$$\begin{aligned} D(T) &= \nabla \cdot (Ke(T) \nabla \cdot T) \\ &= \nabla \cdot \left(Ke(T) \left[\frac{\partial T}{\partial x} \hat{x} + \frac{\partial T}{\partial y} \hat{y} \right] \right) \\ &= \frac{\partial}{\partial x} \left(Ke(T) \frac{\partial T}{\partial x} \right) + \frac{\partial}{\partial y} \left(Ke(T) \frac{\partial T}{\partial y} \right) \end{aligned} \quad (E.5)$$

This equation is simply the 1D case twice and added to each other. This means that we can discretize the equation by using equation 2.72,

$$= \frac{1}{\Delta x^2} \left[\frac{Ke(T)_{i+1} + Ke(T)_i}{2} (T_{i+1} - T_i) + \frac{Ke(T)_{i-1} + Ke(T)_i}{2} (T_{i-1} - T_i) \right] + \quad (E.6)$$

$$\frac{1}{\Delta y^2} \left[\frac{Ke(T)_{j+1} + Ke(T)_j}{2} (T_{j+1} - T_j) + \frac{Ke(T)_{j-1} + Ke(T)_j}{2} (T_{j-1} - T_j) \right] \quad (E.7)$$

Boundary conditions: At the edges we state that the flux outside is zero: $\frac{\partial T}{\partial z} = 0$. For easy calculations we state that the temperature right outside the film is equal to the temperature at the surface.

$$T_{-1} = T_0$$

$$D(T_0) = \frac{1}{\Delta z^2} \left[\frac{Ke(T)_{i+1} + Ke(T)_i}{2} (T_1 - T_0) \right] \quad (\text{E.8})$$

$$T_{i_{max}+1} = T_{i_{max}}$$

$$D(T_{i_{max}}) = \frac{1}{\Delta z^2} \left[\frac{Ke(T)_{i-1} + Ke(T)_i}{2} (T_{i_{max}-1} - T_{i_{max}}) \right] \quad (\text{E.9})$$

In a similar fashion, this goes for the y-direction as well.

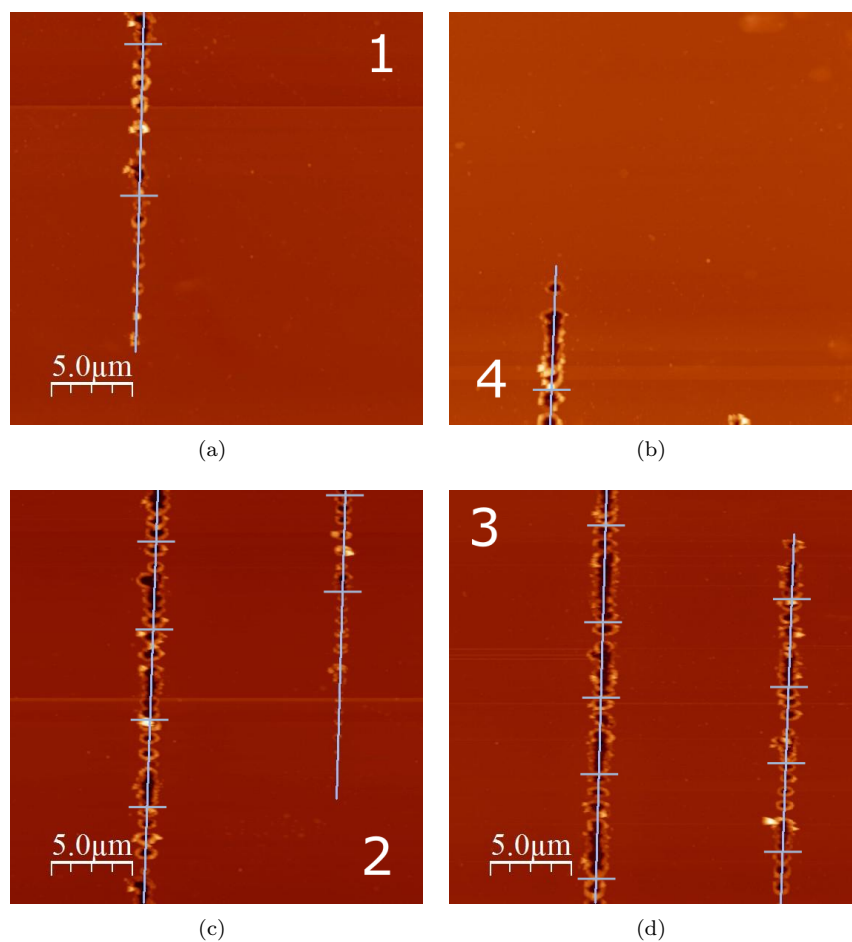


Figure F.0: AFM images of overlapping experiment

F Overlap

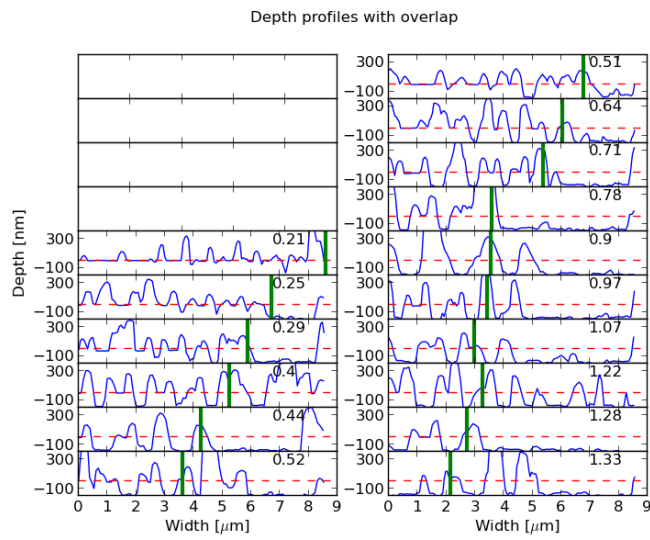


Figure F.1: Depth profile for 20 shots with decreasing intermediate distance ($1 \mu\text{m}$ to $0.05 \mu\text{m}$). Each profile has a different fluence (top right corner).

References

- [1] E. G. Gamaly, S. Juodkakis, K. Nishimura, H. Misawa, B. Luther-Davies, L. Hallo, P. Nicolai, and V. T. Tikhonchuk, "Laser-matter interaction in the bulk of a transparent solid: Confined microexplosion and void formation," *Phys. Rev. B*, vol. 73, p. 214101, Jun 2006.
- [2] M. Li, K. Mori, M. Ishizuka, X. Liu, Y. Sugimoto, N. Ikeda, and K. Asakawa, "Photonic bandpass filter for 1550 nm fabricated by femtosecond direct laser ablation," *Applied Physics Letters*, vol. 83, no. 2, pp. 216–218, 2003.
- [3] P. Pronko, S. Dutta, J. Squier, J. Rudd, D. Du, and G. Mourou, "Machining of sub-micron holes using a femtosecond laser at 800 nm," *Optics Communications*, vol. 114, no. 1-2, pp. 106 – 110, 1995.
- [4] D. van Oosten, M. Spasenović, and L. Kuipers, "Nanohole chains for directional and localized surface plasmon excitation," *Nano Letters*, vol. 10, no. 1, pp. 286–290, 2010. PMID: 20030388.
- [5] S. Anisimov, B. Kapeliovich, and T. Perel'man, "Electron emission from metal surfaces under the action of ultrashort laser pulses," *Zhurnal Eksperimental'noi i Teoreticheskoi Fiziki*, vol. 66, pp. 776 – 781, 1974.
- [6] B. Christensen, K. Vestentoft, and P. Balling, "Short-pulse ablation rates and the two-temperature model," *Applied Surface Science*, vol. 253, no. 15, pp. 6347 – 6352, 2007. Proceedings of the Fifth International Conference on Photo-Excited Processes and Applications (5-ICPEPA).
- [7] K. Yee, "Numerical solution of initial boundary value problems involving maxwell's equations in isotropic media," *IEEE Transactions on Antennas and Propagation*, vol. 14, pp. 302–307, May 1966.
- [8] J. Cheng, C. sheng Liu, S. Shang, D. Liu, W. Perrie, G. Dearden, and K. Watkins, "A review of ultrafast laser materials micromachining," *Optics & Laser Technology*, vol. 46, no. 0, pp. 88 – 102, 2013.
- [9] H. Zhang, D. van Oosten, D. M. Krol, and J. I. Dijkhuis, "Saturation effects in femtosecond laser ablation of silicon-on-insulator," *Applied Physics Letters*, vol. 99, no. 23, p. 231108, 2011.
- [10] D. Sullivan, *Electromagnetic Simulation Using the FDTD Method*. IEEE Press Series on RF and Microwave Technology, Wiley, 2000.
- [11] B. Oliver, "Signal to noise ratios in photoelectric mixing," *Proceedings of the IEEE*, vol. 49, pp. 1960–1961, 1960.
- [12] H. Zhang, *Ablation on Si with a femtosecond laser*. PhD thesis, Utrecht University, 2013.

-
- [13] P. Drude, “Zur Elektronentheorie der Metalle,” *Annalen der Physik*, vol. 306, pp. 566–613, 1900.
- [14] K. Vestentoft and P. Balling, “Formation of an extended nanostructured metal surface by ultra-short laser pulses: single-pulse ablation in the high-fluence limit,” *Applied Physics A*, vol. 84, pp. 207–213, 2006.
- [15] N. J. Berg, *Acousto-optic signal processing: theory and implementation*, vol. 51. CRC Press I Llc, 1996.
- [16] J. Jacobs, “A set-up to measure the influence of split ring resonators on spontaneous emission,” Master’s thesis, Utrecht University, 2009.
- [17] L. Novotny and B. Hecht, *Principles of nano-optics*. Cambridge Press, 2006.